# *Behavior of manufactured sand and recycled coarse aggregate concrete-filled steel tubular stub columns with circular section*

Received: 26 December 2025 | Revised: 28 April 2026 | Accepted: 8 May 2026

DOI: 10.1002/suco.70639

ARTICLE

fib CEB-FIP WILEY

# Behavior of manufactured sand and recycled coarse aggregate concrete-filled steel tubular stub columns with circular section

**Minsheng Guan**[1] | **Qi Chen**[1] | **Gang Wang**[1] | **Aiguo Xiong**[2] | **Ying Wang**[3] | **Le Li**[4] | **Anne W. M. Ng**[5] | **Qing Quan Liang**[4]

[1]Key Laboratory of Coastal Urban Resilient Infrastructures (MOE), Shenzhen University, Shenzhen, China

[2]Transportation Investment & Construction Co., Ltd., China Construction Fourth Engineering Division, Shenzhen, China

[3]College of Civil Engineering, Fuzhou University, Fuzhou, China

[4]College of Sport, Health, and Engineering, Victoria University, Melbourne, Victoria, Australia

[5]School of Science, Technology and Engineering, University of the Sunshine Coast, Sunshine Coast, Queensland, Australia

**Correspondence**
Qing Quan Liang, College of Sport, Health, and Engineering, Victoria University PO Box 14428, Melbourne, VIC 8001, Australia.
Email: qing.liang@vu.edu.au

**Funding information**
National Natiral sicence foundation of China, Grant/Award Numbers: 52278195, 52578222

**Abstract**

Accelerated urbanization has intensified environmental concerns due to excessive natural resource consumption and construction waste generation. Circular concrete-filled steel tube (CFST) columns incorporating manufactured sand recycled coarse aggregate (MS-RCA) concrete have emerged as an innovative composite element offering notable environmental and economic benefits. To advance the use of MS-RCA concrete in CFST structures, this paper presents experimental investigations into the behavior of 72 circular CFST stub columns constructed with MS-RCA concrete. The effects of aggregate type, steel tube thickness, and stone powder content on structural response are examined. The results show that the failure modes of CFST columns with MS-RCA concrete are characterized by local buckling and shear failure, similar to those of circular CFST columns with natural aggregate concrete. CFST columns with MS-RCA have about 5.6% higher ultimate axial strength than those filled with natural sand-RCA concrete. The inclusion of MS significantly enhances the ductility of CFST columns by an average of 34.6%, 25.4%, and 28.6% for steel tube thicknesses of 3.0, 3.5, and 4.0 mm, respectively. Moreover, for high-strength concrete, the ultimate strength of columns filled with pebble MS-RCA concrete is higher than that of those filled with limestone MS-RCA concrete. Existing codes for CFST columns are evaluated and found to be highly conservative. Therefore, a new formula is proposed for CFST columns filled with MS-RCA concrete and validated by experimental data. These findings confirm the viability of CFST columns with MS-RCA concrete and highlight their potential to advance sustainable civil infrastructure.

**KEYWORDS**

concrete-filled steel tube, manufactured sand, recycled coarse aggregate, ultimate strength

## 1 | INTRODUCTION

With the expansion of global infrastructure, concrete has become the most widely used construction material, leading to an enormous demand for natural sand and coarse aggregates.[1] However, the continuous extraction of natural aggregates has led to resource depletion and ecological disturbance. At the same time, rapid urbanization has generated large quantities of construction and demolition waste (CDW). The limited efficiency of current CDW management has further aggravated land occupation and environmental pollution.[2,3] In this context, recycled coarse aggregate (RCA) has been used as an alternative material for concrete production. RAC promotes CDW recycling, alleviates the shortage of natural aggregates, and supports low-carbon and sustainable development.[4,5]

Although RCA concrete offers environmental benefits, its material performance generally differs from that of conventional concrete. Previous studies[6,7] demonstrated that RCA concrete exhibits lower compressive strength, altered long-term mechanical behavior, higher water demand, and inferior durability. These deficiencies are mainly attributed to the presence of adhered old mortar in RCA, as well as its higher porosity, higher crushing index, and weaker interfacial transition zones (ITZs).[8–11] To further reduce the consumption of natural sand, manufactured sand (MS) has also been increasingly adopted as a substitute for natural fine aggregate. Nevertheless, the angular shape, rough surface texture, and variable stone powder content of MS can reduce workability and contribute to variability in compressive strength.[12] These effects arise from increased interparticle friction and surface area, which increase water demand and alter particle packing characteristics.

If the concrete is made with RCA and MS, the resulting material may suffer from cumulative deficiencies unless an effective structural form is adopted to compensate for them. Concrete-filled steel tube (CFST) members provide an effective solution to this challenge. Owing to their high load-bearing capacity, high ductility, and favorable seismic performance, CFST members have been widely adopted in high-rise buildings, bridges, and other critical structures.[13–15] This superior behavior comes from the interaction between the steel tube and the core concrete. The steel tube restrains lateral expansion of the concrete and enhances its strength and deformation capacity. In turn, the core concrete delays local buckling of the steel tube.[16] Therefore, incorporating MS–RCA concrete into CFST columns offers a viable approach to advancing more sustainable concrete materials without significantly compromising structural performance. Moreover, recent studies on advanced hybrid composite columns have further confirmed that enhanced external confinement can effectively improve the ductility and composite action of tubular members incorporating non-conventional concrete. For example, Bai et al.[17] reported favorable compressive behavior of large-size square PEN FRP-concrete-steel hybrid multi-tube concrete columns.

In recent years, the structural behavior of CFST members incorporating recycled or alternative aggregates has received increasing attention. Yang and Ma[18] and Yang et al.[19] investigated RACFST stub columns under axial compression. They reported that the failure modes of RACFST stub columns were similar to those of conventional CFST stub columns. Yang et al.[19] showed that the use of RCA in rectangular CFST columns reduced the stiffness and local stability of the columns. de Azevedo et al.[20] and Zhang et al.[21] demonstrated that RCA can also be used in circular steel tubes with acceptable strength and ductility. However, the axial strength of RACFST stub columns generally decreases as the RCA replacement ratio increases. Ren et al.[22] reported that dune sand concrete-filled steel tubular stub columns under axial compression also exhibited comparable failure modes and satisfactory ductility. The behavior of double-skin tubular stub columns with recycled aggregate concrete and a PET FRP jacket was investigated by Bai et al.[23] It was observed that the tested columns exhibited stable compressive behavior and satisfactory ductility. The study indicated that confinement enhancement is an effective method for mitigating the effects of recycled concrete.

Analytical and numerical studies on the responses of CFST columns with and without recycled aggregate have been undertaken by researchers. Choi and Xiao[24] analytically studied the steel-concrete interaction in circular CFST columns under axial compression. Xu et al.[25] compiled a database of RACFST columns under compression, flexure, and cyclic loads, which can be used to validate numerical models; Chen et al.[26] carried out reliability-based analysis and design factor calibration for circular RACFST stub columns. Nikolić et al.[27] developed a data-driven nonlinear finite-element model for predicting the axial load–displacement response of axially loaded RACFST columns. The above-mentioned studies indicate that the confinement provided by the steel or composite tube can partly offset the disadvantages of recycled or non-traditional aggregates. This was confirmed by recent studies conducted by Jing et al.[28] on large-scale hybrid FRP-concrete-steel double-skin tubular columns under eccentric compression.

Although existing studies have provided important insights into the behavior of RACFST columns, research on circular CFST stub columns filled with concrete made with both MS and RCA remains very limited. As

discussed previously, previous investigations considered only RCA concrete or alternative fine aggregate concrete. The combined use of MS and RCA may alter cracking development, lateral dilation, and confinement efficiency of the infilled concrete. This issue is particularly important for circular CFST stub columns. This is because the uniform confinement provided by the circular steel tube is considerably sensitive to the deformation characteristics of the core concrete. In addition, the combined effects of MS lithology, stone powder content, and steel-tube confinement level have not been quantified experimentally. The studies performed by Lin et al.[29] on hybrid FRP-concrete-steel tubular member T-joints demonstrated that the local transfer of confinement and interaction effects in complex tubular composite systems still relies on a sound understanding of basic member-level behavior. Moreover, no design rules have been proposed in current standards for the design of CFST stub columns filled with MS-RCA concrete.

To address the knowledge gaps identified above, this paper reports an experimental investigation on 72 circular CFST stub columns filled with MS-RCA concrete and subjected to concentric axial compression. The objectives of this study are to: (1) examine the failure modes and axial load-shortening behavior of MS-RCA CFST stub columns for the very first time; (2) quantify the effects of aggregate type, concrete strength, steel-tube thickness, and stone powder content on the performance of MS-RCA CFST stub columns for the first time ever; (3) assess the applicability of existing design codes; and (4) propose a new design formula for predicting the axial strength of circular MS-RCA CFST short columns.

## 2 | EXPERIMENTAL PROGRAM

### 2.1 | Specimen design

Four groups of circular CFST short column specimens were designed and tested. Group I comprised 9 specimens made with concrete incorporating natural sand and natural coarse aggregate. Group II also consisted of 9 specimens employing natural sand and RCA. Group III included 27 specimens using limestone MS combined with RCA, while Group IV comprised 27 specimens with pebble MS and RCA. This grouping enabled a systematic investigation of how fine and coarse aggregate types influence CFST behavior. Comparative analysis across the groups was conducted to clarify how each parameter affects the columns' load bearing capacity and ductility.

The key experimental parameters were aggregate type, concrete strength, steel-tube diameter-to-thickness ratio ($D/t$), and stone-powder content. Regarding aggregate types, four distinct combinations were employed to systematically assess the effects of MS and RCA on structural performance. To study the influence of concrete strength, three grades, C30, C40, and C50, were selected, covering the typical practical range. To investigate the impact of the $D/t$ ratio, the steel tube diameter was fixed at 114 mm while the thicknesses were varied (3.0, 3.5, and 4.0 mm), thereby achieving different $D/t$ ratios. Previous research[30] showed that MS production inevitably yields stone powder (< 75 μm), which can markedly affect concrete performance. Therefore, stone powder content (by mass) was introduced as an additional variable in Groups III and IV. Three levels, 5%, 10%, and 15%, were selected to reflect typical dosages encountered in practice.

All CFST short column specimens were 350 mm in length, yielding a length-to-diameter ratio ($L/D$) of 3.07, meeting the definition of stub columns as specified in current design standards. Detailed specimen configurations are presented in Tables 1–4. The yield strength of steel tube ($f_y$) was 20 MPa. The confining factor ($\xi$) of CFST given in Tables 1–4 was calculated as $\xi = f_y A_s/(f_{ck} A_c)$, where $f_{ck}$ represents the standard axial compressive strength of core concrete, and $A_s$ and $A_c$ represent the cross-sectional areas of steel tube and core concrete, respectively.

Specimens were labeled using an identification code format exemplified by "LR-3.0-C30-5%," where the segments respectively indicate the aggregate combination ("NN" for natural sand-natural coarse aggregate, "NR" for natural sand-RCA, "LR" for limestone MS-RCA, and "PR" for pebble MS-RCA), steel tube thickness in millimeters (e.g., "3.0" indicates 3.0 mm), concrete strength grade, and stone powder content.

### 2.2 | Material properties

This study used Cold-formed circular steel tubes as the external confinement components. To evaluate the mechanical properties of the steel tubes, dog-bone-shaped tensile specimens were fabricated from tubes with thicknesses of 3.0, 3.5 , and 4.0 mm, respectively. The preparation of these specimens followed the Chinese national standard GB/T 228.1-2010,[31] equivalent to the relevant ISO and ASTM standards. Tensile tests were performed using a 300 kN MTS universal testing machine to determine the material properties. Cold-formed Q235 steel had elastic modulus $E_s = 206$ GPa, yield strength $f_y = 320$ MPa, and ultimate tensile strength $f_u = 440$ MPa. The core concrete was designed with three strength grades: C30, C40, and C50. The compressive strength tests were conducted in accordance with the Chinese standard GB/T 50081-2019.[32] P.O 42.5R (ordinary Portland cement) was used for all mixes. The fine aggregates included natural river sand, limestone MS, and

**TABLE 1** Details of specimens in Group I.

| Specimen ID | $D \times t$ (mm) | $D/t$ | $f_{cu}$ (MPa) | ξ | $N_u$ (kN) | DI (ductility index) |
|---|---|---|---|---|---|---|
| NN-3.0-C30 | 114 × 3.0 | 38.0 | 44.4 | 1.23 | 899.09 | 2.31 |
| NN-3.5-C30 | 114 × 3.5 | 32.6 | 44.4 | 1.46 | 990.39 | 4.12 |
| NN-4.0-C30 | 114 × 4.0 | 28.5 | 44.4 | 1.69 | 1096.65 | 2.83 |
| NN-3.0-C40 | 114 × 3.0 | 38.0 | 53.7 | 1.02 | 948.73 | 2.26 |
| NN-3.5-C40 | 114 × 3.5 | 32.6 | 53.7 | 1.20 | 1028.01 | 1.60 |
| NN-4.0-C40 | 114 × 4.0 | 28.5 | 53.7 | 1.40 | 1130.02 | 1.71 |
| NN-3.0-C50 | 114 × 3.0 | 38.0 | 65.4 | 0.86 | 995.80 | 3.70 |
| NN-3.5-C50 | 114 × 3.5 | 32.6 | 65.4 | 1.02 | 1004.23 | 2.25 |
| NN-4.0-C50 | 114 × 4.0 | 28.5 | 65.4 | 1.18 | 1004.23 | 2.21 |

**TABLE 2** Details of specimens in Group II.

| Specimen ID | $D \times t$ (mm) | $D/t$ | $f_{cu}$ (MPa) | ξ | $N_u$ (kN) | DI (ductility index) |
|---|---|---|---|---|---|---|
| NR-3.0-C30 | 114 × 3.0 | 38.0 | 31.3 | 1.75 | 745.52 | 2.67 |
| NR-3.5-C30 | 114 × 3.5 | 32.6 | 31.3 | 2.07 | 833.98 | 5.01 |
| NR-4.0-C30 | 114 × 4.0 | 28.5 | 31.3 | 2.39 | 910.12 | 4.39 |
| NR-3.0-C40 | 114 × 3.0 | 38.0 | 41.8 | 1.31 | 834.30 | 1.80 |
| NR-3.5-C40 | 114 × 3.5 | 32.6 | 41.8 | 1.55 | 879.23 | 2.17 |
| NR-4.0-C40 | 114 × 4.0 | 28.5 | 41.8 | 1.79 | 964.90 | 2.24 |
| NR-3.0-C50 | 114 × 3.0 | 38.0 | 52.7 | 1.07 | 842.13 | 1.94 |
| NR-3.5-C50 | 114 × 3.5 | 32.6 | 52.7 | 1.27 | 920.10 | 2.84 |
| NR-4.0-C50 | 114 × 4.0 | 28.5 | 52.7 | 1.47 | 1026.70 | 2.70 |

pebble MS, all with a fineness modulus of 2.7. The natural coarse aggregate was continuously graded crushed limestone (5–31.5 mm). RCA, obtained from demolished bridge piers and beams, was crushed, screened, washed, and dried before replacing natural coarse aggregate. A high-performance polycarboxylate-based superplasticizer was added to improve the workability of the concrete. The detailed mix proportions of the core concrete are listed in Table 5.

Concrete mixing followed standard procedures to ensure uniformity. First, the fine aggregate and cement were dry-mixed in a mixer for 1 min. The coarse aggregate was then added and mixed for another minute. Finally, water and superplasticizer were introduced, followed by 2 min of mixing. The fresh concrete was immediately cast into 100 mm × 100 mm × 100 mm cube molds and compacted on a vibrating table until no visible air bubbles remained on the surface. After 24 h, the specimens were demolded and cured under standard conditions (temperature: 20 ± 2°C; relative humidity ≥95%) for 28 days prior to compressive strength testing. The measured cubic compressive strength ($f_{cu}$) values are provided in Tables 1–4.

The test results showed that the type of aggregate significantly impacted the compressive strength of the concrete. Under the same water-cement ratio and curing conditions, concrete made with limestone MS exhibited slightly higher strength than that made with natural sand (Figure 1a). This is primarily attributed to the angular and rough surfaces of MS particles, which improve ITZ properties. This phenomenon has been referred to as the morphological effect of MS.[33] In addition, the compressive strength of concrete incorporating RCA was consistently lower than that of concrete made with natural coarse aggregate (Figure 1b), with reductions of 29.5%, 22.2%, and 19.4% for different strength grades. This reduction is mainly due to the presence of more microcracks and higher porosity in RCAs, which can lead to stress concentrations under load and reduce the overall bearing capacity. These findings are consistent with those reported in related studies.[34]

## 2.3 | Loading and measurement schemes

Axial compression tests were performed using a YAW 6306 electro-hydraulic machine with a maximum capacity of 3000 kN. The loading setup is shown in Figure 2.

**TABLE 3** Details of specimens in Group III.

| Specimen ID | $D \times t$ (mm) | $D/t$ | $\alpha$ (%) | $f_{cu}$ (MPa) | $\xi$ | $N_u$ (kN) | DI (ductility index) |
|---|---|---|---|---|---|---|---|
| LR-3.0-C30-5% | 114 × 3.0 | 38.0 | 5 | 35.6 | 1.53 | 813.49 | 3.19 |
| LR-3.5-C30-5% | 114 × 3.5 | 32.6 | 5 | 35.6 | 1.82 | 883.25 | 4.07 |
| LR-4.0-C30-5% | 114 × 4.0 | 28.5 | 5 | 35.6 | 2.11 | 999.91 | 4.67 |
| LR-3.0-C30-10% | 114 × 3.0 | 38.0 | 10 | 32.6 | 1.68 | 767.49 | 4.37 |
| LR-3.5-C30-10% | 114 × 3.5 | 32.6 | 10 | 32.6 | 1.98 | 846.27 | 5.29 |
| LR-4.0-C30-10% | 114 × 4.0 | 28.5 | 10 | 32.6 | 2.30 | 960.54 | 5.28 |
| LR-3.0-C30-15% | 114 × 3.0 | 38.0 | 15 | 33.3 | 1.64 | 740.83 | 3.95 |
| LR-3.5-C30-15% | 114 × 3.5 | 32.6 | 15 | 33.3 | 1.94 | 851.51 | 5.27 |
| LR-4.0-C30-15% | 114 × 4.0 | 28.5 | 15 | 33.3 | 2.25 | 959.10 | 5.58 |
| LR-3.0-C40-5% | 114 × 3.0 | 38.0 | 5 | 45.5 | 1.20 | 858.99 | 2.13 |
| LR-3.5-C40-5% | 114 × 3.5 | 32.6 | 5 | 45.5 | 1.42 | 962.15 | 3.12 |
| LR-4.0-C40-5% | 114 × 4.0 | 28.5 | 5 | 45.5 | 1.65 | 1018.81 | 3.58 |
| LR-3.0-C40-10% | 114 × 3.0 | 38.0 | 10 | 43.8 | 1.25 | 865.88 | 2.97 |
| LR-3.5-C40-10% | 114 × 3.5 | 32.6 | 10 | 43.8 | 1.48 | 867.38 | 3.23 |
| LR-4.0-C40-10% | 114 × 4.0 | 28.5 | 10 | 43.8 | 1.71 | 1047.37 | 3.44 |
| LR-3.0-C40-15% | 114 × 3.0 | 38.0 | 15 | 46.2 | 1.18 | 849.10 | 3.35 |
| LR-3.5-C40-15% | 114 × 3.5 | 32.6 | 15 | 46.2 | 1.40 | 922.67 | 3.84 |
| LR-4.0-C40-15% | 114 × 4.0 | 28.5 | 15 | 46.2 | 1.62 | 1001.18 | 3.63 |
| LR-3.0-C50-5% | 114 × 3.0 | 38.0 | 5 | 53.0 | 1.07 | 877.33 | 2.41 |
| LR-3.5-C50-5% | 114 × 3.5 | 32.6 | 5 | 53.0 | 1.26 | 980.25 | 3.26 |
| LR-4.0-C50-5% | 114 × 4.0 | 28.5 | 5 | 53.0 | 1.46 | 1036.33 | 3.78 |
| LR-3.0-C50-10% | 114 × 3.0 | 38.0 | 10 | 54.6 | 1.03 | 898.88 | 3.00 |
| LR-3.5-C50-10% | 114 × 3.5 | 32.6 | 10 | 54.6 | 1.22 | 962.42 | 3.36 |
| LR-4.0-C50-10% | 114 × 4.0 | 28.5 | 10 | 54.6 | 1.42 | 1069.62 | 4.06 |
| LR-3.0-C50-15% | 114 × 3.0 | 38.0 | 15 | 57.9 | 0.98 | 923.13 | 2.80 |
| LR-3.5-C50-15% | 114 × 3.5 | 32.6 | 15 | 57.9 | 1.15 | 1017.31 | 3.20 |
| LR-4.0-C50-15% | 114 × 4.0 | 28.5 | 15 | 57.9 | 1.34 | 1078.33 | 3.00 |

Before formal loading, a preload of 3 kN was applied and then removed to eliminate any gaps between the specimen and the loading platens and to confirm the readiness of the testing apparatus. Based on existing literature[35–37] and testing standards,[38] a combined load–displacement control protocol was adopted. In the initial loading stage, load-controlled incremental loading was implemented in steps of 100 kN, with each load level maintained for 2 min at a loading rate of 1 kN/s. Once the applied load reached 75% of the predicted ultimate bearing capacity, the control mode was switched to displacement control at 3 mm/min. Tests ended when the axial load fell to 85% of its peak or the LVDTs reached full stroke; ultimate axial capacities were then predicted using the formulas in Reference [39].

During the axial compression tests, strain gauges, a 3000 kN column-type load cell, and LVDTs were used to capture real-time data on strain, axial load, and axial displacement of the short column specimens. Strain gauges were employed to measure longitudinal and circumferential strains of the steel tube (Figure 3a). Four sets of strain gauges were evenly spaced around the outer surface at mid-height of the steel tube, with each set consisting of two gauges: one for measuring longitudinal (axial) strain and the other for transverse (hoop) strain. Additionally, two axial strain gauges were affixed to the front and rear surfaces near the ends of the steel tube to measure end strains at the tube ends. The axial load was measured using the 3000 kN load cell placed beneath the specimen, which moved upward in coordination with the lower loading platen during testing. Four 50 mm-range LVDTs at the plate corners recorded axial displacement. The configuration of the measurement instrumentation is illustrated in Figure 3b.

**TABLE 4** Details of specimens in Group IV.

| Specimen ID | $D \times t$ (mm) | $D/t$ | $\alpha$ (%) | $f_{cu}$ (MPa) | $\xi$ | $N_u$ (kN) | DI |
|---|---|---|---|---|---|---|---|
| PR-3.0-C30-5% | 114 × 3.0 | 38.0 | 5 | 31.9 | 1.71 | 781.10 | 3.99 |
| PR-3.5-C30-5% | 114 × 3.5 | 32.6 | 5 | 31.9 | 2.03 | 888.57 | 4.01 |
| PR-4.0-C30-5% | 114 × 4.0 | 28.5 | 5 | 31.9 | 2.35 | 967.57 | 4.26 |
| PR-3.0-C30-10% | 114 × 3.0 | 38.0 | 10 | 29.4 | 1.86 | 744.81 | 3.02 |
| PR-3.5-C30-10% | 114 × 3.5 | 32.6 | 10 | 29.4 | 2.20 | 848.68 | 3.58 |
| PR-4.0-C30-10% | 114 × 4.0 | 28.5 | 10 | 29.4 | 2.55 | 962.53 | 4.52 |
| PR-3.0-C30-15% | 114 × 3.0 | 38.0 | 15 | 28.7 | 1.90 | 737.04 | 3.57 |
| PR-3.5-C30-15% | 114 × 3.5 | 32.6 | 15 | 28.7 | 2.25 | 844.94 | 3.80 |
| PR-4.0-C30-15% | 114 × 4.0 | 28.5 | 15 | 28.7 | 2.61 | 977.33 | 4.01 |
| PR-3.0-C40-5% | 114 × 3.0 | 38.0 | 5 | 40.7 | 1.34 | 842.45 | 2.86 |
| PR-3.5-C40-5% | 114 × 3.5 | 32.6 | 5 | 40.7 | 1.59 | 903.28 | 3.80 |
| PR-4.0-C40-5% | 114 × 4.0 | 28.5 | 5 | 40.7 | 1.84 | 1016.63 | 4.76 |
| PR-3.0-C40-10% | 114 × 3.0 | 38.0 | 10 | 43.2 | 1.26 | 864.14 | 2.44 |
| PR-3.5-C40-10% | 114 × 3.5 | 32.6 | 10 | 43.2 | 1.50 | 931.05 | 2.80 |
| PR-4.0-C40-10% | 114 × 4.0 | 28.5 | 10 | 43.2 | 1.73 | 1058.24 | 4.37 |
| PR-3.0-C40-15% | 114 × 3.0 | 38.0 | 15 | 45.5 | 1.20 | 874.64 | 2.39 |
| PR-3.5-C40-15% | 114 × 3.5 | 32.6 | 15 | 45.5 | 1.42 | 925.49 | 3.07 |
| PR-4.0-C40-15% | 114 × 4.0 | 28.5 | 15 | 45.5 | 1.65 | 999.34 | 3.76 |
| PR-3.0-C50-5% | 114 × 3.0 | 38.0 | 5 | 52.7 | 1.07 | 924.54 | 2.56 |
| PR-3.5-C50-5% | 114 × 3.5 | 32.6 | 5 | 52.7 | 1.27 | 1008.31 | 3.08 |
| PR-4.0-C50-5% | 114 × 4.0 | 28.5 | 5 | 52.7 | 1.47 | 1103.55 | 3.64 |
| PR-3.0-C50-10% | 114 × 3.0 | 38.0 | 10 | 50.3 | 1.12 | 939.37 | 2.65 |
| PR-3.5-C50-10% | 114 × 3.5 | 32.6 | 10 | 50.3 | 1.33 | 1025.08 | 3.20 |
| PR-4.0-C50-10% | 114 × 4.0 | 28.5 | 10 | 50.3 | 1.54 | 1097.62 | 3.09 |
| PR-3.0-C50-15% | 114 × 3.0 | 38.0 | 15 | 54.2 | 1.04 | 935.32 | 2.88 |
| PR-3.5-C50-15% | 114 × 3.5 | 32.6 | 15 | 54.2 | 1.23 | 1036.19 | 2.79 |
| PR-4.0-C50-15% | 114 × 4.0 | 28.5 | 15 | 54.2 | 1.43 | 1140.37 | 3.03 |

## 3 | EXPERIMENTAL OBSERVATIONS AND RESULTS

### 3.1 | Failure processes and modes

The damage evolution and failure modes of the circular CFST short column specimens were continuously monitored throughout the entire loading process and recorded using a high-resolution digital video camera. Based on the observed phenomena, the failure process of the specimens can be categorized into four distinct stages: the linear-elastic stage, elastic–plastic stage, yielding stage, and strengthening stage. In the linear-elastic stage, specimens exhibited negligible deformation, axial and hoop strains increased linearly with axial load, and slight rust peeling occasionally appeared. During the elastic–plastic stage, closer inspection revealed minor local buckling of the steel tube. The rate of strain development, both longitudinal and transverse, increased and deviated from linearity, indicating the onset of plastic behavior. In the yielding stage, local buckling intensified and cracking sounds signaled progressive core concrete crushing as the specimen approached peak load $N_u$. During the strengthening stage, buckling of the steel tube developed rapidly, with additional localized buckling observed near the specimen ends in some cases. The test was terminated when the axial displacement reached approximately 30 mm.

Figure 4 presents the final failure modes and damage characteristics of representative specimens. It was observed that specimens filled with MS-RCA concrete exhibited failure patterns similar to those of conventional circular CFST stub columns, predominantly characterized by pronounced outward local buckling. Based on the observed damage configurations at failure, two primary failure modes were identified: (1) Drum-shaped failure:

**TABLE 5** Mix proportions of concrete.

| Concrete type | Concrete strength grade | $\alpha$ (%) | Water-cement ratio | Content (kg/m$^3$) | | | | | Sand ratio (%) |
|---|---|---|---|---|---|---|---|---|---|
| | | | | Cement | Water | Sand | Gravel | Water reducer | |
| NN (NR) | C30 | 0 | 0.5 | 407 | 204 | 666 | 958 | 0.81 | 41 |
| | C40 | 0 | 0.37 | 538 | 199 | 596 | 932 | 2.69 | 39 |
| | C50 | 0 | 0.32 | 609 | 195 | 563 | 919 | 6.09 | 38 |
| LR (PR) | C30 | 5 | 0.5 | 407 | 204 | 633 | 958 | 0.81 | 41 |
| | C30 | 10 | 0.5 | 407 | 204 | 599 | 958 | 0.81 | 41 |
| | C30 | 15 | 0.5 | 407 | 204 | 566 | 958 | 0.81 | 41 |
| | C40 | 5 | 0.37 | 538 | 199 | 566 | 932 | 2.69 | 39 |
| | C40 | 10 | 0.37 | 538 | 199 | 536 | 932 | 2.69 | 39 |
| | C40 | 15 | 0.37 | 538 | 199 | 507 | 932 | 2.69 | 39 |
| | C50 | 5 | 0.32 | 609 | 195 | 535 | 919 | 6.09 | 38 |
| | C50 | 10 | 0.32 | 609 | 195 | 507 | 919 | 6.09 | 38 |
| | C50 | 15 | 0.32 | 609 | 195 | 479 | 919 | 6.09 | 38 |

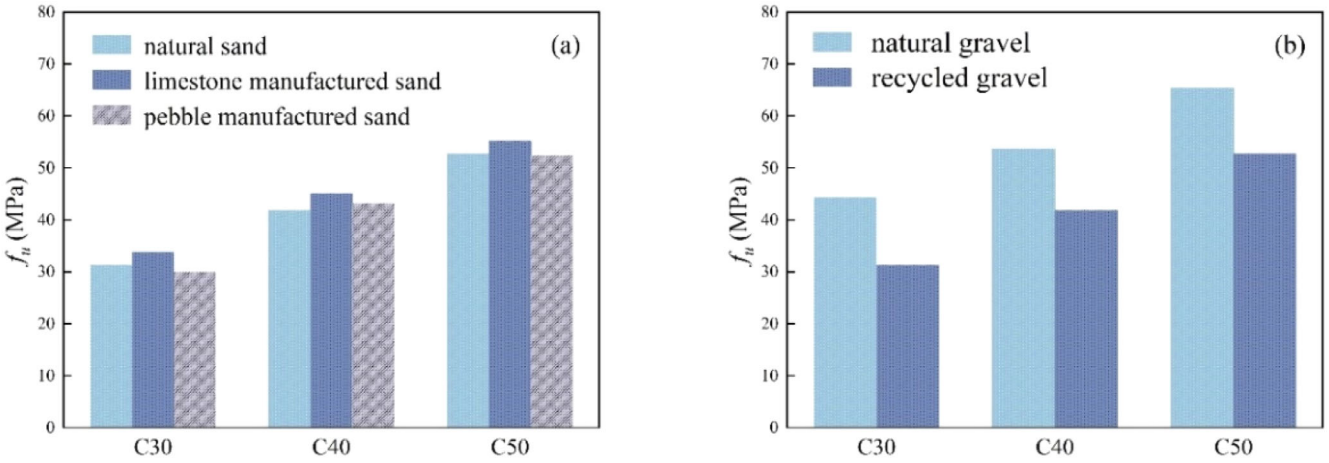


**FIGURE 1** The impact of types of fine/coarse aggregate on the compressive strength of concrete: (a) types of fine aggregate (b) types of coarse aggregate.

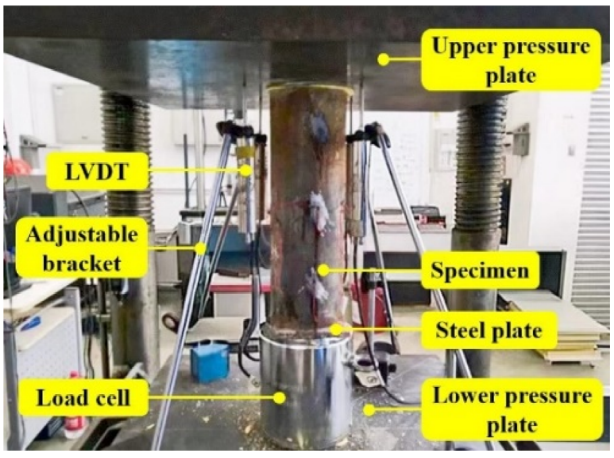


**FIGURE 2** Schematic diagram of the loading system.

Axial loading caused lateral expansion of the core concrete and outward deformation of the confining steel tube. Bulging formed near mid-height or ends, resembling a drum shape. (2) Shear-type failure: When confinement was insufficient, local buckling occurred in weaker tube regions, triggering diagonal shear cracking in the core concrete and simultaneous failure of the buckling of the steel tube.

Notably, a few specimens with high-strength core concrete and relatively thin-walled steel tubes experienced localized tensile stress concentrations during axial compression. When the steel tube's local bearing capacity was insufficient to withstand these stresses, the tube yielded or tore, ultimately leading to crack formation and rupture.

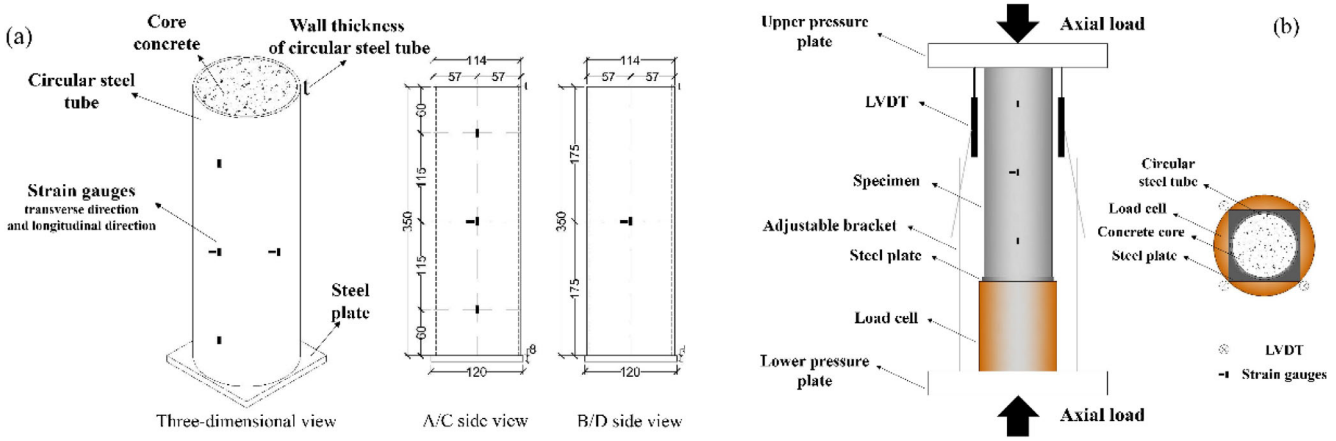


**FIGURE 3** Measurement system diagram: (a) strain gauge arrangement; (b) location of load cell and LVDTs.

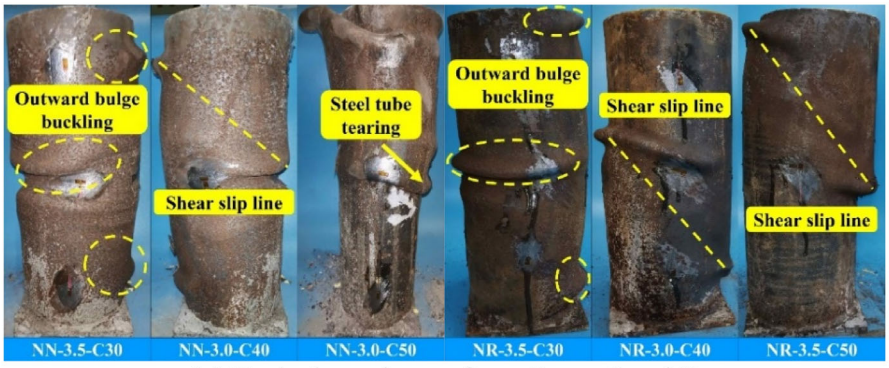


(a) Typical specimens from Group I and II

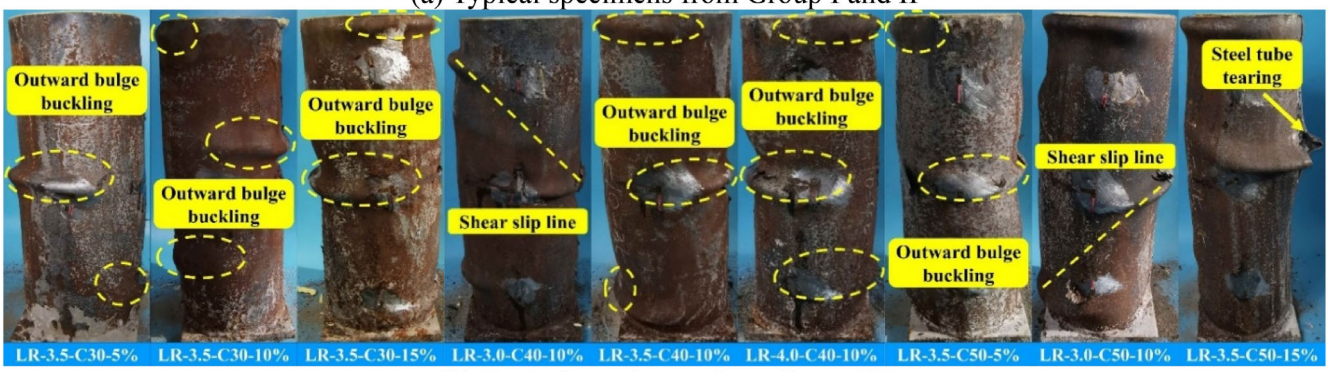


(b) Typical specimens from Group III

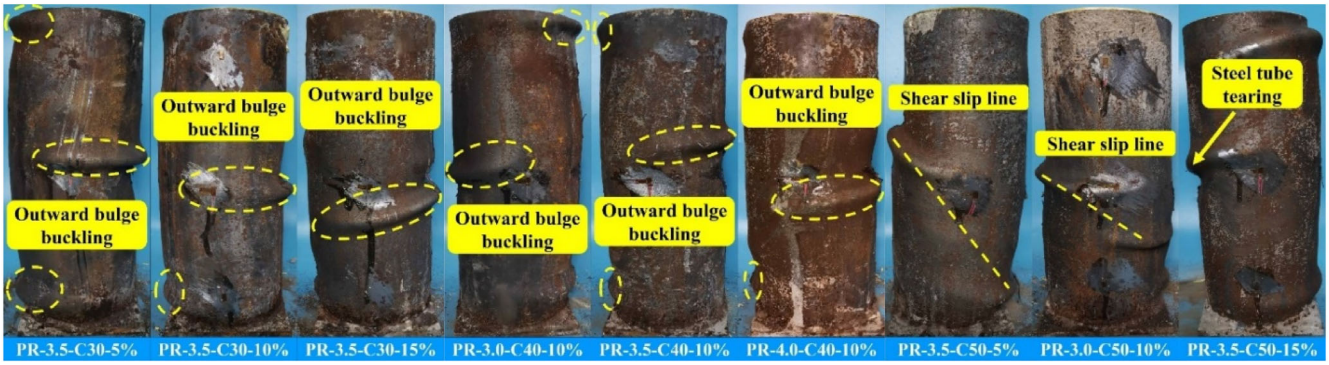


(c) Typical specimens from Group IV

**FIGURE 4** Final failure mode of representative CFST specimens.

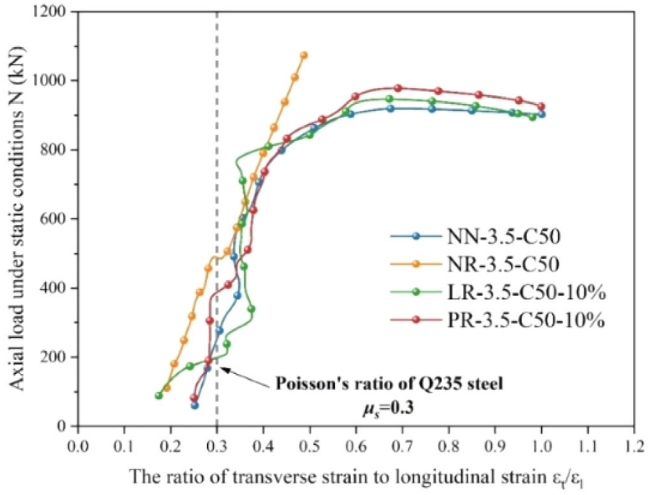


**FIGURE 5** Axial load-lateral deformation coefficient curves of CFST specimens.

After classifying failure modes, steel tube confinement on the core concrete was further analyzed. It was characterized by the lateral deformation coefficient, defined as the ratio of transverse strain to longitudinal strain. The coefficient was averaged from four strain gauge rosettes placed at mid-height along the outer wall of the steel tube.

As shown in Figure 5, representative lateral deformation coefficient curves were selected for comparative analysis. Except for specimens filled with natural sand-RCA concrete, the remaining specimens exhibited similar evolutionary trends.

In the initial stage, the core concrete's lower Poisson's ratio resulted in negligible confinement. The lateral deformation coefficient remained close to the steel's Poisson's ratio, indicating that both materials were in an unconfined uniaxial compression state.

When the axial load reached approximately 60%–70% of the peak capacity $N_u$, cracking initiated in the core concrete. At this point, its lateral deformation exceeded that of the steel tube, resulting in the activation of confinement. The lateral deformation coefficient increased rapidly. As loading progressed and cracking intensified, steel tube confinement strengthened, leading to a plateau in the deformation coefficient curve.

Under identical design parameters and confinement conditions, Circular CFST columns with MS-RCA concrete specimens exhibited slightly higher axial load capacity compared to specimens filled with natural aggregate concrete. Notably, the lateral deformation coefficient curves for natural sand-RCA filled specimens lacked stabilization in later loading stages. This suggests that the steel tube's confinement was not fully mobilized. The primary reason is attributed to the rough surface texture of the RCA, which retains remnants of old mortar, resulting in a weak ITZ.[40] Furthermore, the higher porosity and pronounced local stress concentrations of RCA concrete promoted early crack initiation, thereby limiting the activation of effective confinement.

In contrast, the incorporation of MS improved the ITZ properties, enhancing the concrete's density and strain compatibility. As a result, both load bearing capacity and deformation performance were significantly improved.

## 3.2 | Load-axial shortening curves

The axial load-axial shortening ($N$–△) curves for all specimens are presented in Figure 6. The axial shortening values were obtained by averaging the measurements from four LVDTs. Based on the analysis of these curves, the typical load-shortening response of the circular CFST stub columns can be divided into four characteristic stages:

(1) *Linear-elastic stage*: In this initial stage, the outer steel tube and the core concrete bore certain portions of the axial load independently, with negligible overall deformation. Due to the lower Poisson's ratio of the core concrete compared to the steel tube, no significant confinement is exerted at this stage. The $N$–△ curve displays a linear relationship, reflecting the combined elastic behavior of the two components.

(2) *Elastic–plastic stage*: As the axial load approached approximately 70% of the peak load ($N_u$), the elastic modulus of the steel tube decreased, and microcracking developed in the core concrete with lateral expansion. Local buckling of the steel tube became visible. At this point, the steel tube began to provide lateral confinement, and the core concrete started transiting into a triaxial compression state. Consequently, the $N$–△ curve began to deviate from linearity and displayed clear nonlinear behavior.[41]

(3) *Post-peak descending stage*: After the specimen reached the peak load ($N_u$), the interaction between the external steel tube and the core concrete evolved further. As the axial load increases, the longitudinal stress in the core concrete became much greater than the hoop stress, ultimately leading to pronounced bulging or shear failure. For many specimens, a sharp load drop was observed immediately after reaching the peak load. This brief decline is attributed to insufficient confinement from the steel tube, causing a reduction in load bearing capacity. During this stage, the steel tube primarily sustained lateral stresses, while its contribution to axial load resistance diminished.

(4) *Strengthening stage*: In this phase, the steel tube entered the strengthening region, and its confinement

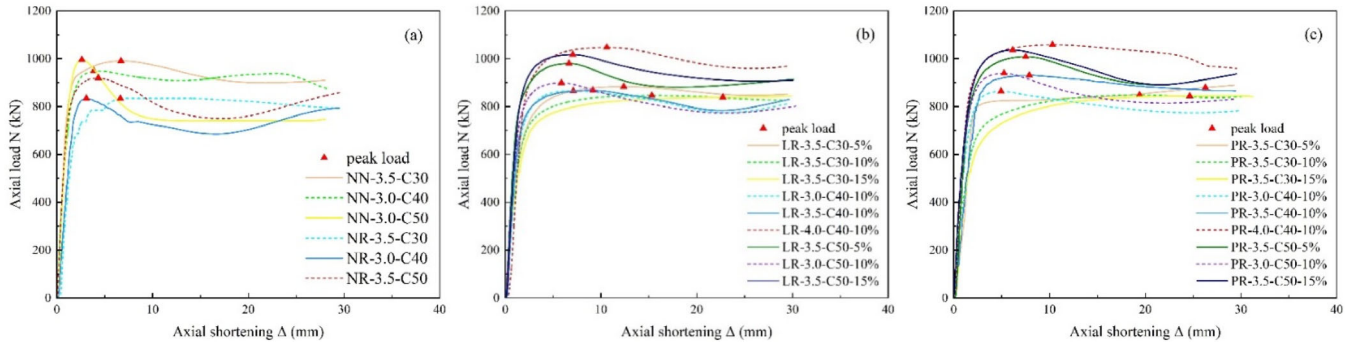


**FIGURE 6** Axial load-axial shortening curve of representative CFST specimens: (a) Group I and II, (b) Group III, (c) Group IV.

effect on the core concrete became increasingly prominent. Therefore, the lateral confinement force slowed the propagation of cracks and delayed further damage within the concrete core. As a result, a partial recovery in load bearing capacity was observed, and some specimens exhibited a secondary peak in the $N$–$\triangle$ curve.[42] However, this secondary peak remained lower than the initial peak $N_u$. Beyond this point, axial shortening increased rapidly, load carrying capacity plateaued or slightly declined, and the specimen ultimately failed due to excessive deformation.

A comparative analysis of the load-shortening ($N$–$\triangle$) curves across the four groups of specimens revealed the following performance trends: (1) Group I: Lower initial stiffness than Group II but a higher peak load. Several specimens showed a sharp post-peak drop, reflecting limited ductility. (2) Group II: Exhibited the highest initial stiffness with a smooth and stable ascending branch. After reaching the peak load, the curves showed a gradual post-peak decline. Some specimens demonstrated a secondary rise at larger displacements, indicating substantial residual load bearing capacity beyond peak load. (3) Group III: Displayed slightly lower initial stiffness compared to Group I but exhibited an extended plateau region in the post-peak stage. In some cases, a secondary load increase was observed, suggesting enhanced plastic deformation capacity and better energy dissipation after peak load. (4) Group IV: Demonstrated the highest overall peak load among the groups. Although some descending branches were steep, most specimens exhibited a combination of high load-carrying capacity and good ductility, indicating superior overall performance under axial compression.

## 4 | EFFECTS OF PARAMETERS ON AXIAL STRENGTHS

Axial compression tests on CFST stub columns were conducted to assess the impact of four key parameters: fine aggregate type, coarse aggregate type, steel tube thickness, and stone powder content.

### 4.1 | Influence of fine aggregate type

As listed in Tables 1–4, CFST stub columns filled with concrete made using MS exhibited, on average, a 5.6% higher axial compressive capacity than those using natural sand. This enhancement is primarily attributed to the angular shape and rough surface texture of MS particles, improving the packing density and compactness of the core concrete. This phenomenon is commonly referred to as the morphological effect of MS,[33] although such advantages may be less prominent under the complex triaxial stress states imposed by the steel tube confinement. Additionally, the higher surface roughness and porosity of MS[43] may enhance the interfacial bonding between the aggregate and the cement paste, further contributing to the improved axial capacity.

Experimental data further revealed that for C30 and C40 concrete, stub columns filled with limestone MS concrete exhibited relatively better axial capacity, primarily due to the regular particle shape and moderate surface roughness, which enhanced interfacial bonding. In contrast, for higher strength grade (C50), stub columns incorporating pebble MS performed better. The lower water-to-cement ratios of high-strength concrete magnified the benefits of the higher density and compressive strength of pebble MS, thereby enhancing axial load bearing capacity.

### 4.2 | Influence of coarse aggregate type

Under identical design parameters, CFST specimens filled with RCA concrete exhibited slightly lower axial capacity compared to those filled with natural coarse aggregate. This reduction in capacity can be related to

two primary factors: (1) RCA typically retains residual old mortar on its surface,[8] which may prevent stress transfer and hinder void filling within the concrete matrix; (2) although the lateral confinement provided by the steel tube effectively suppresses the expansion of the core concrete, the higher prevalence of microcracks in RCA,[44] collectively undermining the composite action and resulting in a net reduction in axial performance.

Further comparative analysis revealed that the adverse impact of RCA on axial capacity diminished with increasing concrete strength grade. Specifically, the reductions in axial capacity associated with RCA were approximately 16.6% at low strength, 13.7% at medium strength, and 11.8% at high strength levels. These findings indicate that the confining effect of the steel tube becomes increasingly effective in mitigating the deficiencies of RCA as the concrete strength increases.

### 4.3 | Influence of steel tube thickness

Increasing the thickness of the steel tube markedly improved the axial compressive capacity of the CFST stub columns. An increase from 3.0 to 4.0 mm led to an average increase of about 20.8% in the axial capacity. This improvement is mainly attributed to the enhanced lateral confinement provided by thicker steel tubes. Under axial loading, the core concrete tends to expand laterally, and the steel tube, through its hoop confinement, restricts this deformation, placing the concrete into a triaxial compressive stress state, thereby significantly improving strength and ductility.

Moreover, the test results indicate that increasing steel tube thickness has a more pronounced effect on the behavior of low-strength concrete (e.g., C30), for which the steel tube contributes a greater proportion of the total load bearing capacity. Conversely, in high-strength concrete, which already has high axial capacity, the marginal benefit of thicker tubes diminishes because the concrete itself carries a larger share of the load.

### 4.4 | Influence of stone powder content

The axial capacities varied slightly across stone powder levels. Experimental findings suggest that a moderate amount of stone powder improves the gradation of MS and fills inter-particle voids, an effect commonly referred to as the micro-filler effect.[45] This results in improved compactness of the core concrete, which in turn enhances the axial compressive capacity. However, excessive stone powder content may disrupt the optimal particle packing structure, leading to reduced mechanical performance.

After optimization, the axial compressive capacity of CFST columns filled with MS-RCA concrete increased by approximately 7% compared to other specimens within the same group. Additionally, high-strength concrete exhibited the best axial performance at relatively low stone powder contents. This may be due to the higher binder content in such mixes, where excessive stone powder can adversely affect the ITZ, thereby reducing the overall compressive performance.[46]

## 5 | EFFECTS OF PARAMETERS ON DUCTILITY

To examine the influence of various parameters on CFST column ductility, the ductility index (DI), which is determined as the ratio of ultimate displacement ($\Delta u$) to yield displacement ($\Delta y$) defined by Park[47] was adopted. Experimental DI values are summarized in Tables 1–4, with key parameter effects discussed below.

### 5.1 | Influence of fine aggregate type

As observed in Tables 1–4, CFST stub columns filled with limestone MS concrete and pebble MS concrete exhibited significantly higher ductility than those filled with natural sand concrete. Analysis of the test data revealed that when the steel tube thickness was 3.0, 3.5, and 4.0 mm, the DI increased by an average of 34.6%, 25.4%, and 28.6%, respectively. This improvement is due to the angular shape and rough surface texture of MS, which enhance the interfacial bond between the aggregate and the cement paste, thereby improving the deformability of the composite section.

However, when the concrete strength grade increased to C50, the difference in ductility between natural sand and MS concrete became negligible. This suggests that the influence of fine aggregate type diminishes with increasing concrete strength. The reduced sensitivity may be attributed to the more brittle nature of high-strength concrete, where failure behavior is predominantly governed by the cementitious matrix and the ITZ rather than by aggregate morphology.[48]

### 5.2 | Influence of coarse aggregate type

On average, specimens incorporating RCA exhibited moderately higher ductility than those with natural coarse aggregate, with the DI increasing by approximately 15.5%. The improvement in ductility for specimens incorporating RCA can be attributed to its intrinsic

material properties (such as strength and ductility) of RCA. The higher porosity and lower elastic modulus of RCA allow for greater plastic deformation under loading, while internal pores and microcracks contribute to energy dissipation and delay the propagation of major cracks. The confinement provided by the external steel tube imposes a triaxial compressive stress state on the core concrete, further hindering crack development. As a result, these combined factors allow RCA concrete specimens to retain a higher deformation capacity post-peak loading, resulting in superior ductility compared to specimens with natural coarse aggregate. Similar findings have been reported in previous studies.[49]

### 5.3 | Influence of steel tube thickness

When the thickness increased from 3.0 to 4.0 mm, the DI improved by approximately 16.6%. This enhancement is primarily attributable to the greater confinement afforded by thicker steel tubes, which restrain the lateral expansion of the core concrete, limit crack propagation, and mitigate stress concentrations, thereby improving overall deformation capacity.

Increasing steel tube thickness enhances the circumferential confinement of the core concrete, promoting a more pronounced triaxial compressive stress state and delaying crack development, while also increasing the critical stress for local buckling of the steel tube. As a result, thicker steel tubes prolong the plastic deformation stage, enabling the specimen to dissipate more energy through the combined effects of steel yielding and crack closure in the concrete. However, a few specimens deviate from the general trend due to local tearing of the steel tube during the loading process.

### 5.4 | Influence of stone powder content

Overall, no clear trend was observed, suggesting that the influence of stone powder content on ductility is insignificant within the test range. This may be attributed to the fact that the stone powder content in all specimens was maintained within a reasonable limit, thus failing to induce substantial changes in the mechanical behavior of the core concrete. As a result, ductility differences among specimens lack discernible regularity.

From a microstructural perspective, an appropriate amount of stone powder can act as a micro-filler to improve the pore structure of MS concrete,[45] reducing harmful pores and increasing gel pores, thereby enhancing the compactness of the matrix and potentially contributing to improved ductility. However, due to its low reactivity, excessive stone powder may accumulate in the ITZ, weakening matrix-aggregate bonds and impairing the concrete's mechanical properties.

Previous studies[50] have also indicated that the enhancement of ductility by stone powder is relatively limited and highly dependent on multiple factors, such as the properties of raw materials and the concrete mix design. Therefore, in CFST structures incorporating MS as the fine aggregate, stone powder content should be optimized in conjunction with other mixture parameters. Since this study did not include microscopic morphological analysis of concrete, future research may employ scanning electron microscopy or pore structure characterization techniques to further investigate the underlying relationship between stone powder dosage and concrete ductility.

## 6 | CALCULATION OF AXIAL COMPRESSIVE CAPACITY

### 6.1 | Comparison of experimental results and code predictions

This section assessed the applicability of key design codes for predicting the axial compressive capacity of circular CFST stub columns filled with MS-RCA concrete. Globally, many design specifications for CFST structures have been developed, and their calculation methodologies can be broadly classified into two theoretical categories.

The Unified Theory, proposed by Zhong et al.[51] treats steel tubes and concrete core as a single composite material and does not differentiate their individual contributions. The axial load bearing capacity is calculated as the product of the total composite cross-sectional area and an equivalent compressive strength. A representative example of this approach is the Chinese specification GB 50936-2014[38] (referred to herein as the "GB code"). The Superposition Theory assumes that steel tubes and concrete core contribute independently to the overall capacity. In this approach, the axial capacities of the steel and concrete components are calculated separately and then summed up to obtain the total capacity. Notable examples include ANSI/AISC 360-16[52] (referred to as the "AISC code"), AIJ-2008[53] (referred to as the "AIJ code"), and BS EN 1994-1-1:2004[54] (referred to as the "EC4 code").

Using the design equations from the four codes, the axial compressive capacities of specimens filled with limestone MS-RCA concrete and pebble MS-RCA concrete were calculated and compared with the experimental values (Figure 7).

As illustrated in Figure 7, the experimentally measured-to-predicted capacity ratio ($N_{u,e}/N_{u,c}$) ranged

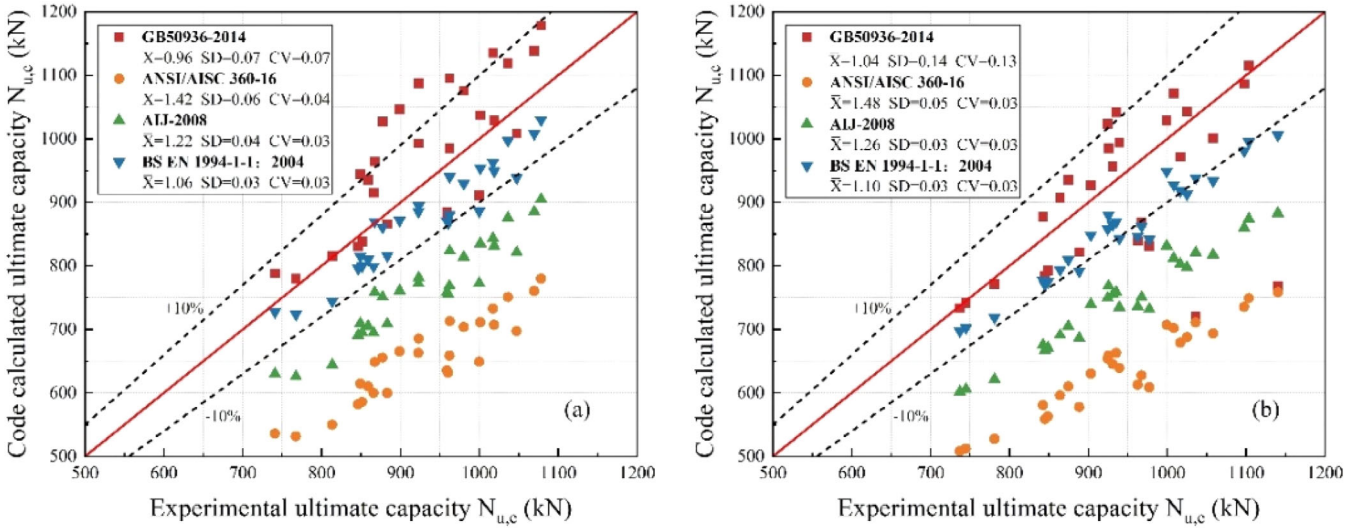


**FIGURE 7** Comparison between the code calculated ultimate bearing capacities with the test data of circular CFST columns with MS-RCA concrete: (a) limestone MS (b) pebble MS.

**FIGURE 8** Performance of revised formula.

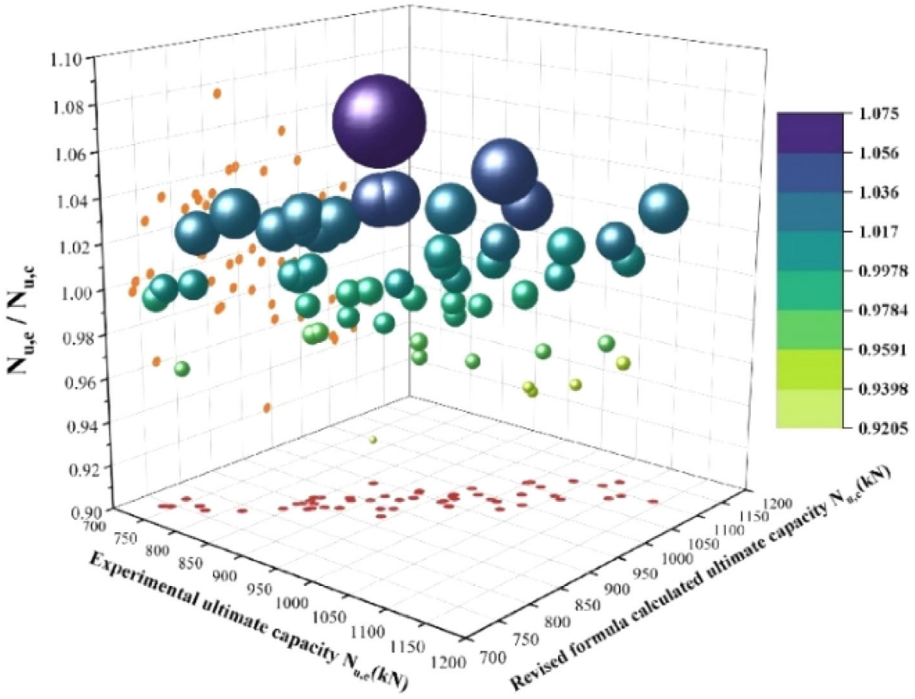


from 0.96 to 1.48, indicating that all four design codes yielded safe and reasonably conservative predictions. Among these, the GB Code, which is based on the Unified Theory, exhibited the closest agreement with the experimental results. However, it also recorded the largest coefficient of variation, 11.8%, indicating a comparatively wide dispersion in its predictions.

In contrast, the three Superposition Theory codes underestimated the axial compressive capacity. This underestimation is primarily attributable to their inadequate consideration of the beneficial confinement afforded by RCA in the core concrete. The largest deviation occurred in the AISC Code, which underestimated the axial capacity by an average of approximately 31% relative to the experimental results. From a consistency standpoint, predictions generated by the AISC, AIJ, and EC4 Codes exhibited lower variability, with coefficients of variation between 3% and 4%, indicating tighter clustering of results but at the expense of reduced accuracy. In addition to codified approaches, advanced techniques such as machine learning have also been employed to predict the ultimate axial compressive capacity of CFST columns, demonstrating promising potential for improving prediction accuracy.[55]

## 6.2 | Proposed design formula

This study proposed a modified design formula to enhance applicability and more accurately capture the synergistic strength of MS and RCA in CFSTs. The equation was derived by refining Han's analytical framework[56] within the Unified Theory.

The modified formula proposed in this study is expressed as follows:

$$Nu = fck(a + b\xi)(As + Ac) \quad (1)$$

$$\xi = \frac{As \cdot fy}{Ac \cdot fck} \quad (2)$$

The applicable parameter ranges for the modified equations are: $f_{ck} = 16.72–35.59$ MPa, $\xi = 0.95–2.65$, $f_y = 235–420$ MPa. Based on the experimental data obtained in this study, a multiple linear regression analysis was conducted to calibrate the coefficients of the modified formula. The optimal values were determined as: $a = 0.77$ and $b = 1.61$.

The regression yielded a high coefficient of determination ($R^2 = 0.97$), indicating a strong correlation between the predicted and experimental results. The improved formula produced an average predicted-to-experimental capacity ratio of 0.9995, with a standard deviation of 0.0307, demonstrating excellent agreement with the test data. These results confirm that the proposed formula offers an accurate and reliable method for estimating the axial compressive capacity of circular CFST columns with MS-RCA concrete. The detailed comparison is illustrated in Figure 8.

Given the limited research on CFST columns incorporating both MS and RCA, future work should include additional experimental tests and numerical simulations to further validate and refine the proposed formula.

## 7 | CONCLUSIONS

This paper has presented an experimental study on the performance of axially loaded short circular CFST columns made with manufactured sand-recycled coarse aggregate (MS-RCA) concrete. The structural behavior and failure modes of these stub columns under axial compression have been investigated. The effects of aggregate type, steel tube thickness, and stone powder content on the strength and ductility of CFST columns have been analyzed. A formula has been proposed for the design of circular CFST stub columns made with MS-RCA concrete. Based on the experimental results, the following conclusions are drawn:

(a) MS-RCA infilled circular CFST stub columns showed failure modes comparable to those with natural aggregate concrete, dominated by outward local buckling; shear-type failure and occasional tube tearing occurred more frequently in specimens with higher concrete strength.

(b) Compared with the natural sand RCA concrete counterparts under comparable configurations, MS-RCA infilled CFST stub specimens achieved an average increase of approximately 5.6% in ultimate axial capacity.

(c) Using MS significantly improved deformation capacity. Relative to the NR specimens, the DI increased on average by 34.6%, 25.4%, and 28.6% for steel tube thicknesses of 3.0, 3.5, and 4.0 mm, respectively; the improvement became less pronounced for the higher-strength concrete mixes. Within the investigated range, the effect of stone powder content on ductility was secondary.

(d) For the high-strength mixes considered, pebble MS-RCA infill resulted in marginally higher peak loads than limestone MS-RCA infill, while both infills exhibited comparable ductility. These results indicate that substituting limestone MS-RCA with pebble MS-RCA in high-strength CFST columns can enhance their axial compressive capacity without compromising deformation capacity.

(e) Existing design codes provided conservative predictions for MS-RCA infilled circular CFST stub columns. The proposed formula is shown to accurately predict the ultimate axial strengths of CFST short columns filled with MS-RCA concrete.

## NOMENCLATURE

| | |
|---|---|
| $A_c$ | cross-sectional area of concrete infill |
| $A_s$ | cross-sectional area of steel tube |
| CDW | construction and demolition waste |
| CFST | concrete-filled steel tube |
| $D$ | outer diameter of circular steel tube |
| $E_s$ | elastic modulus of steel |
| $f_{ck}$ | compressive strength of concrete |
| $f_{cu}$ | cubic strength of concrete |
| $f_u$ | tensile strength of steel |
| $f_y$ | yield strength of steel |
| ITZ | interfacial transition zone |
| $L$ | length of CFST column |
| LR | limestone manufactured sand recycled coarse aggregate concrete |
| NN | natural sand natural coarse aggregate concrete |
| NR | natural sand recycled coarse aggregate concrete |
| $N$ | axial load under static conditions |
| $N_u$ | ultimate bearing capacity of concrete-filled steel tube under axial compression |

$N_{u,c}$ calculated ultimate axial strength of CFST column
$N_{u,e}$ Experimental ultimate axial strength of CFST column
PR pebble manufactured sand recycled coarse aggregate concrete
$t$ wall thickness of steel tube
$\alpha$ stone powder content
$\Delta$ axial displacement measured value
$\Delta_{max}$ measured axial displacement corresponding to the ultimate load
$\Delta u$ ultimate axial displacement of the specimen
$\Delta y$ axial displacement at yield of the specimen

## AUTHOR CONTRIBUTIONS

**Minsheng Guan:** Conceptualization, methodology, investigation, visualization, funding acquisition; **Qi Chen:** Software, data curation, visualization, writing-original draft; **Gang Wang:** Data curation, writing-original draft; **Aiguo Xiong:** Investigation, conceptualization, validation; **Ying Wang:** Methodology, validation; **Le Li:** Writing-review and editing, visualization; **Anne W. M. Ng:** Writing-review and editing, visualization; **Qing Quan Liang:** Writing-review and editing, supervision.

## ACKNOWLEDGMENTS

This work was supported by the National Natural Science Foundation of China (Grant No. 52278195 and 52578222). The financial support is gratefully acknowledged. Open access publishing facilitated by Victoria University, as part of the Wiley - Victoria University agreement via the Council of Australasian University Librarians

## CONFLICT OF INTEREST STATEMENT

The authors declare that they have no known competing financial interests or personal relationships that could have appeared to influence the work reported in this paper.

## DATA AVAILABILITY STATEMENT

The data that support the findings of this study are available from the corresponding author upon reasonable request.

## ORCID

*Minsheng Guan* https://orcid.org/0000-0002-8884-0316
*Ying Wang* https://orcid.org/0000-0001-6366-550X
*Anne W. M. Ng* https://orcid.org/0000-0002-7698-9068
*Qing Quan Liang* https://orcid.org/0000-0003-0333-2265

## REFERENCES

1. Xiao J, Zou S, Poon CS, Sham ML, Li Z, Shah SP. We use 30 billion tonnes of concrete each year—here's how to make it sustainable. Nature. 2025;638(8052):888–90.
2. He X, Gao W, Guan D, Zhou L. Impacts of urban shrinkage on the built environment and its environmental sustainability: An analytical review. Environ Res Lett. 2023;18(10):103004.
3. Akhtar A, Sarmah AK. Construction and demolition waste generation and properties of recycled aggregate concrete: a global perspective. J Clean Prod. 2018;186:262–81.
4. Yu B, Wang J, Li J, Lu W, Li CZ, Xu X. Quantifying the potential of recycling demolition waste generated from urban renewal: a case study in Shenzhen, China. J Clean Prod. 2020;247:119127.
5. Tam VWY, Soomro M, Evangelista ACJ. A review of recycled aggregate in concrete applications (2000–2017). Construct Build Mater. 2018;172:272–92.
6. Guo H, Shi C, Guan X, Zhu J, Ding Y, Ling T-C, et al. Durability of recycled aggregate concrete—a review. Cem Concr Compos. 2018;89:251–9.
7. Silva R, de Brito J, Dhir R. The influence of the use of recycled aggregates on the compressive strength of concrete: a review. Eur J Environ Civ Eng. 2015;19(7):825–49.
8. Xiao J, Li J, Sun Z, Hao X. Study on compressive strength of recycled aggregate concrete. Tongji Daxue Xuebao/J Tongji Univ. 2004;12:1558–61.
9. Wang Q, Geng Y, Wang Y, Zhang H. Drying shrinkage model for recycled aggregate concrete accounting for the influence of parent concrete. Eng Struct. 2020;202:109888.
10. Tabsh SW, Abdelfatah AS. Influence of recycled concrete aggregates on strength properties of concrete. Construct Build Mater. 2009;23(2):1163–7.
11. Shi XS, Collins EG, Zhao XL, Wang QY. Mechanical properties and microstructure analysis of fly ash geopolymeric recycled concrete. J Hazard Mater. 2012;237:20–9.
12. Jadhav PA, Kulkarni DK. Effect of replacement of natural sand by manufactured sand on the properties of cement mortar. Int J Civ Struct Eng. 2013;3(3):621.
13. Hajjar JF. Concrete-filled steel tube columns under earthquake loads. Progr Struct Eng Mater. 2000;2(1):72–81.
14. Inai E, Mukai A, Kai M, Tokinoya H, Fukumoto T, Mori K. Behavior of concrete-filled steel tube beam columns. J Struct Eng. 2004;130(2):189–202.
15. Song TY, Li CL, Chen Z, Liu XL, Zhou HY. Post-fire performance of axially-loaded elliptical concrete-filled steel tubular stub columns. Structure. 2023;50:2004–23.
16. Ahmed M, Shahin RI, Yehia SA, Emara M, Patel VI, Liang QQ. Nonlinear analysis of square steel-reinforced concrete-filled steel tubular short columns considering local buckling. Struct Concr. 2024;25(1):69–84.
17. Bai Y-L, Mei S-J, Chan C-W, Li Q-Q. Compressive behavior of large-size square PEN FRP-concrete-steel hybrid multi-tube concrete columns. Eng Struct. 2021;246:113017.
18. Yang YF, Ma GL. Experimental behaviour of recycled aggregate concrete filled stainless steel tube stub columns and beams. Thin-Walled Struct. 2013;66:62–75.
19. Yang D, Liu F, Wang Y. Axial compression behaviour of rectangular recycled aggregate concrete-filled steel tubular stub columns. J Constr Steel Res. 2023;201:107687.
20. de Azevedo VS, de Lima LR, Vellasco PCS, Tavares MEN, Chan T-M. Experimental investigation on recycled aggregate concrete filled steel tubular stub columns under axial compression. J Constr Steel Res. 2021;187:106930.
21. Zhang X, Zhu Y, Zhang W, Kong W, Lin Y, Chen Y. Research on axial compression performance of recycled aggregate

concrete-filled steel tubular column. J Constr Steel Res. 2025; 229:109541.
22. Ren QX, Zhou K, Hou C, Tao Z, Han LH. Dune sand concrete-filled steel tubular (CFST) stub columns under axial compression: experiments. Thin-Walled Struct. 2018;124:291–302.
23. Bai Y-L, Zhang Y-F, Jia J-F, Han Q, Gao W-Y. Compressive behavior of double-skin tubular stub columns with recycled aggregate concrete and a PET FRP jacket. Construct Build Mater. 2022;332:127321.
24. Choi KK, Xiao Y. Analytical studies of concrete-filled circular steel tubes under axial compression. J Struct Eng. 2010;136(5): 565–73.
25. Xu J, Wang Y, Ren R, Wu Z, Ozbakkaloglu T. Performance evaluation of recycled aggregate concrete-filled steel tubes under different loading conditions: database analysis and modelling. J Build Eng. 2020;30:101308.
26. Chen W, Xu J, Li Z, Huang X, Wu Y. Load-carrying capacity of circular recycled aggregate concrete-filled steel tubular stub columns under axial compression: reliability analysis and design factor calibration. J Build Eng. 2023;66:105935.
27. Nikolić J, Tošić N, Murcia-Delso J, Kostić SM. Data-driven nonlinear finite element modelling of stub recycled aggregate concrete-filled steel tube columns under axial compression. Construct Build Mater. 2025;505:144755.
28. Jiang T, Lin G, Xie P. Behavior of large-scale hybrid FRP-concrete-steel double-skin tubular columns subjected to eccentric compression. Eng Struct. 2023;275:115258.
29. Lin G, Zeng J, Li J, Chen G, Zhou J. Behavior of hybrid FRP-concrete-steel double-skin tubular member T-joints subjected to brace axial compression. Thin-Walled Struct. 2024;202: 112081.
30. Kang JT, Chen XX, Yu ZC. Effect of polypropylene fiber on frost resistance and carbonation resistance of manufactured sand concrete. Structure. 2023;56:16.
31. GB/T 228.1-2021. Metallic materials-tensile testing-part 1: method of test at room temperature. Beijing: China Architecture & Building Press; 2022.
32. GB/T 50081-2019. Standard for test methods of concrete physical and mechanical properties. Beijing: China Architecture & Building Press; 2019.
33. Han Z, Zhang Y, Zhang W, Qiao H, Feng Q, Xue C, et al. Study on comprehensive morphological parameters of manufactured sand based on CT scanning and entropy method and its application in rheology of manufactured sand mortar. Construct Build Mater. 2023;370:130628.
34. Poon CS, Shui ZH, Lam L. Effect of microstructure of ITZ on compressive strength of concrete prepared with recycled aggregates. Construct Build Mater. 2004;18(6):461–8.
35. Chen ZP, Xu JJ, Xue JY, Su YS. Performance and calculations of recycled aggregate concrete-filled steel tubular (RACFST) short columns under axial compression. Int J Steel Struct. 2014;14(1):31–42.
36. Wang YY, Chen P, Liu CY, Zhang Y. Size effect of circular concrete-filled steel tubular short columns subjected to axial compression. Thin-Walled Struct. 2017;120:397–407.
37. Wang J, Li Z, Cai J, Jin B. Axial compression performance of slurry-wrapping recycled aggregate concrete-filled steel tube short columns under freeze-thaw cycles. Struct Concr. 2025; 26(3):3416–29.
38. GB 50936-2014. Technical code for concrete filled steel tubular structures. Beijing: China Architecture & Building Press; 2014.
39. Cai S, Jiao Z. Basic performance and strength calculation of concrete filled steel tubular hollow short column. J Build Struct. 1984;06:13–29.
40. Lu D, Wang D, Wang Y, Zhong J. Nano-engineering the interfacial transition zone between recycled concrete aggregates and fresh paste with graphene oxide. Construct Build Mater. 2023; 384:131244.
41. Luo SC, Chen MC, Huang H, Xv K, Fang W, Zhang R. Eccentric compression test and ultimate load strength analysis of circular CFST long column with local corrosion. Structure. 2023;56:18.
42. Ke X-J, Chen Z-P, Su Y-S, Xue J-Y. Mechanical performance and ultimate bearing capacity of steel reinforced high-strength concrete shear wall under cyclic reveresd loading. Eng Mech. 2014;31(9):126–32.
43. Zhang Y, An MZ, Han B, Wang JW, Wang Y. Multi-parameter mix proportion design and optimization of manufactured sand concrete based on RSM. Structure. 2025;73:14.
44. He W, Kong X, Fu Y, Zhou C, Zheng Z. Experimental investigation on the mechanical properties and microstructure of hybrid fiber reinforced recycled aggregate concrete. Construct Build Mater. 2020;261:120488.
45. Zhou A, Miao G, Zhang Y, Qian R, Zhang Y, Shi J, et al. Effects of stone powder on microstructure of manufactured-sand concrete and its gas permeability. J Build Eng. 2024;91:109539.
46. Li F, Yao T, Luo J, Song Q, Yang T, Zhang R, et al. Experimental investigation on the performance of ultra-high performance concrete (UHPC) prepared by manufactured sand: mechanical strength and micro structure. Construct Build Mater. 2024;452: 139001.
47. Park R. Ductility evaluation from laboratory and analytical testing. Proceedings of the 9th world conference on earthquake engineering. Tokyo-Kyoto, Japan: Association for Earthquake Disaster Prevention; 1988.
48. Liu J, Ma K, Shen J, Zhu J, Long G, Xie Y, et al. Influence of recycled concrete aggregate enhancement methods on the change of microstructure of ITZs in recycled aggregate concrete. Construct Build Mater. 2023;371:130772.
49. Wang J, Li Z, Jin B. Axial compression behavior and stress-strain relationship of slurry-wrapping treatment recycled aggregate concrete-filled steel tube short columns. Rev Adv Mater Sci. 2023;62(1):20230117.
50. Li H, Wang Z, Sun R, Huang F, Yi Z, Yuan Z, et al. Effect of different lithological stone powders on properties of cementitious materials. J Clean Prod. 2021;289:125820.
51. Kuranovas A, Goode D, Kvedaras AK, Zhong ST. Load-bearing capacity of concrete-filled steel columns. J Civ Eng Manag. 2009;15(1):21–33.
52. ANSI/AlSC 360–16. American Institute of Steel Construction. Specification for structural steel buildings. Chicago: American Institute of Steel Construction; 2016.
53. AIJ-2008. Recommendations for design and construction of concrete filled steel tubular structures. Tokyo: Architectural Institute of Japan; 2008.
54. BS EN 1994-1-1:2004. European Committee for Standardization. Eurocode 4: Design of Composite Steel and Concrete Structures-Part 1-1:general rules and rules for buildings. Brussels: European Committee for Standardization; 2004.

55. Tran V-L, Ahmed M, Gohery S. Prediction of the ultimate axial load of circular concrete-filled stainless steel tubular columns using machine learning approaches. Struct Concr. 2023;24(3): 3908–32.
56. Han LH. Concrete filled steel tubular structures—theory and practice. 3rd ed. Beijing: Science Press; 2016.

## AUTHOR BIOGRAPHIES

**Minsheng Guan**, Key Laboratory of Coastal Urban Resilient Infrastructures (MOE), Shenzhen University, Shenzhen 518060, China. Email: msguan@szu.edu.cn.

**Qi Chen**, Key Laboratory of Coastal Urban Resilient Infrastructures (MOE), Shenzhen University, Shenzhen 518060, China. Email: chenqi2023@email.szu.edu.cn.

**Gang Wang**, Key Laboratory of Coastal Urban Resilient Infrastructures (MOE), Shenzhen University, Shenzhen 518060, China. Email: wanggang3669@163.com.

**Aiguo Xiong**, Transportation Investment & Construction Co., Ltd., China Construction Fourth Engineering Division, Shenzhen 518052, China. Email: kp20082008@126.com.

**Ying Wang**, College of Civil Engineering, Fuzhou University, Fuzhou 350116, China. Email: wangying763@fzu.edu.cn.

**Le Li**, College of Sport, Health, and Engineering, Victoria University, PO Box 14428, Melbourne, VIC 8001, Australia. Email: le.li@vu.edu.au.

**Anne W. M. Ng**, School of Science, Technology and Engineering, University of the Sunshine Coast, Queensland, Australia. Email: wng@usc.edu.au.

**Qing Quan Liang**, College of Sport, Health, and Engineering, Victoria University, PO Box 14,428, Melbourne, VIC 8001, Australia. Email: qing.liang@vu.edu.au.

**How to cite this article:** Guan M, Chen Q, Wang G, Xiong A, Wang Y, Li L, et al. Behavior of manufactured sand and recycled coarse aggregate concrete-filled steel tubular stub columns with circular section. Structural Concrete. 2026. https://doi.org/10.1002/suco.70639